2024 IEEE International Conference on Robotics and Automation (ICRA 2024)
May 13-17, 2024. Yokohama, Japan

Modeling and Analysis of Combined Rimless Wheel with Tensegrity Spine

Yuxuan Xiang[1], Yanqiu Zheng[2] and Fumihiko Asano[1]

***Abstract*— In the natural world, benefited from the advantages of the spine, quadrupeds exhibiting extraordinary flexibility which allowing them to move efficiently on variable terrains. The previous researches have indicated the legged robots which efficiently utilizing their spine can achieve rapid and stable locomotion. However, within the field of legged robot dynamics, the design of the spine and understanding how it positively influences locomotion is unclear, which is significant for quadruped robot to achieve efficient and stable walking. In this study, we proposed a model formed by tensegrity spine and rimless wheel to represent quadrupeds, using passive dynamic walking as a method, which has been well-demonstrated for observing the inherent characteristics, exhibited the locomotion characteristic of the model proposed. By numerical simulation, we observed change trend of locomotion performance with the configurations of spine's shape, and found direction of spine design that have a positive impact on walking. These findings contribute to the design of spine structures in quadruped robots.**

I. INTRODUCTION

In the natural world, vertebrates possess the capability to change stiffness of spine to enhance load-bearing capacity or flexibility. Especially in the case of quadrupeds, which can efficiently locomotes on the flat ground. Comparing to bipedal humans, quadrupeds are good at to leverage the advantages of their spine, exhibiting extraordinary efficient running capabilities. For example, after tens of thousands of years of evolution, the cheetah has achieved an unparalleled terrestrial speed. This kind of locomotion is also considered to be the most energy-efficient mode of locomotion for quadrupeds [1]. From the perspective of elastic energy storage, the benefits of spine extension in vertebrates for high-speed motion have been studied [2]. In previous studies, the combination of legged robots and compliant spines can produce reasonably fast and stable locomotion gaits [3], [4]. It has been discovered that the synchronization of leg and spine movements can enhance locomotion speed and stability [5], [6].

On the other hand, in biomechanical studies, a biological spine is composed of rigid structures (skeletal framework) and flexible muscular tissues [7], [8]. In the absence of external forces, the entire structure remains in equilibrium.

This research was partially supported by Grant-in-Aid for Scientific Research (C) No. 23K03727, provided by the Japan Society for the Promotion of Science (JSPS).

[1]Yuxuan Xiang and Fumihiko Asano are with the Graduate School of Advanced Science and Technology, Japan Advanced Institute of Science and Technology, 1-1 Asahidai, Nomi, Ishikawa 923-1292, Japan {kouuken,fasano}@jaist.ac.jp

[2]Yanqiu Zheng is with the Department of Mechanical Engineering, Ritsumeikan University, 1-1-1 Nojihigashi, Kusatsu Shiga 525-8577, Japan zhengyq@fc.ritsumei.ac.jp

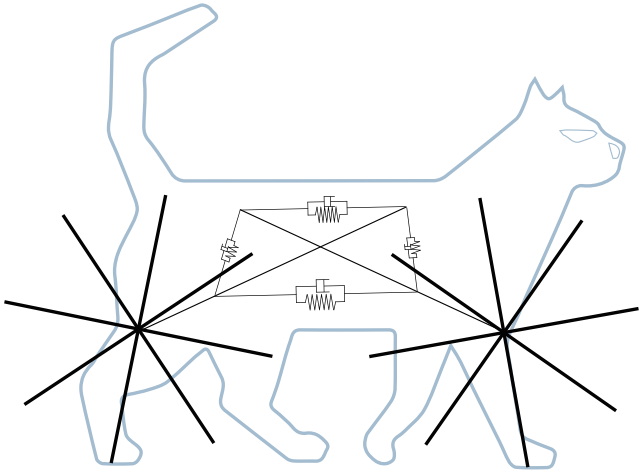

Fig. 1. Conceptual drawing of quadruped represented by combined rimless wheel with tensegrity spine

As same as the biological spine, the tensegrity structures are also combined by rigid components and soft cables [9], [10]. The past researches has demonstrated the flexibility and practicality of tensegrity spine structures [11], [12], however, the dynamics of tensegrity spines have not been extensively studied. Therefore, in this study, we aim to investigate the dynamics of tensegrity spine, and to analyze the influence of spine structure on the locomotion performance. By recognizing that the walking of quadrupeds is the inverted pendulum-like motion generated by forelimbs and hindlimbs, respectively [13]–[15]. In this study, we used the rimless wheel of simplest walking model, which is capable of producing typical inverted pendulum motion, to represent the forelimbs and hindlimbs of quadrupeds. As shown in Fig. 1, two rimless wheels are connected utilizing the tensegrity spine proposed to form a quadrupeds model.

Moreover, passive walking was proposed by McGeer in 1990 [16] to mimic a human gait with no input during downhill, relying only on the conversion between gravitational potential energy and kinetic energy. It can autonomously transform the gravitational potential energy into the kinetic energy of the system through the its own structure to achieve a stable gait [17]. Conclusively, the structure will greatly determine the dynamics of itself. In this study we exhibit the characteristic of the model itself by passive walking.

In this paper, we proposed the simplest model of tensegrity spine, and by combining 2 identical rimless wheels, formed a combined rimless wheels, to represent the quadruped. The design of the shape of tensegrity spine is clarified. To analyzed influence of the spine shape on locomotion capabilities, the simulation conducted using the shape of the

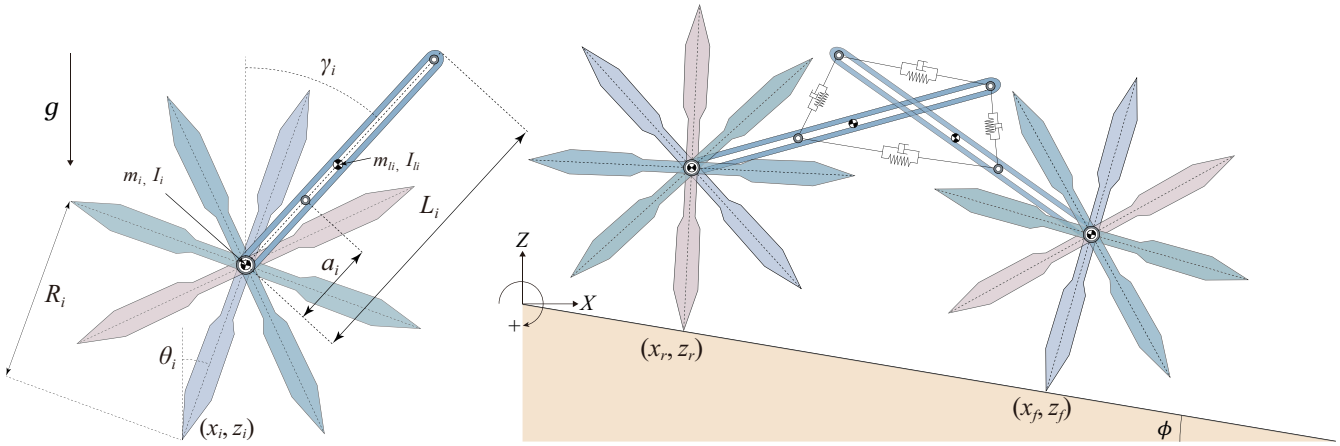

(a) Coordinate system for each rimless wheel with upper body

(b) Conbined rimless wheel passive walking on the gentle downhill

Fig. 2. Mathematical model of combined rimless wheel with tensegrity spine

tensegrity spine structure as a variable and walking speed as a performance metric. It was observed that models utilizing the spine structure could achieve stable passive walking, and vibrations were detected on the spine. Subsequently, the impact of the weight proportion between the legs and spine on walking performance is observed.

II. MODELING

A. Overview of Modeling

Fig. 2 (a) illustrates the coordinate system of the rimless wheel with a upper body, where (x_i, z_i) denote the position of the ground contact points, θ_i represents the rotation angular position of rimless wheel to the vertical direction. Additionally, when we remove the soft cables from the spine, the model can be viewed as two rimless wheels with an upper body. The γ_i denotes the rotation angle position of the upper body to the vertical direction. In the context, the R_i [m] is the radius of the rimless wheel, which equates with the leg length of the quadruped. m_i [kg] and I_i [kg·m^2] represent the mass and inertial moment of the rimless wheel, respectively. The length of the upper body is L_i [m] with its mass and moment of inertia being m_l [kg] and I_l [kg·m^2], respectively. The a_i [m] is the distance from passive rotation joint of upper body to the first connection point of soft cable. In addition, the second connection point is on the top of the upper body. The subscripts i shall represent the rimless wheel mark, that is, $i \in \{f, r\}$, with "f" and "r" specifically indicating the front and rear wheels, respectively. The combined rimless wheel models Fig. 2 (b), which walks on a gentle downhill with a slope angle of ϕ [rad].

B. Equation of Motion

The model can be viewed as being composed of two wheel-less robots with upper bodies, which are coupled through tensile forces. Therefore, the generalized coordinates vector can be denoted as:

$\boldsymbol{q} = \begin{bmatrix} x_r & z_r & \theta_r & \gamma_r & x_f & z_f & \theta_f & \gamma_f \end{bmatrix}^{\mathrm{T}}$, the system's equation of motion and holonomic constraint condition then become:

$$\boldsymbol{M}\ddot{\boldsymbol{q}} + \boldsymbol{h} = \boldsymbol{J}_c^{\mathrm{T}}\boldsymbol{\lambda}_c + \boldsymbol{J}_T^{\mathrm{T}}\boldsymbol{F}_T, \tag{1}$$

$$\boldsymbol{J}_c\dot{\boldsymbol{q}} = \boldsymbol{0}_{4\times 1}, \tag{2}$$

where $\boldsymbol{M}$ represents the inertia matrix, $\boldsymbol{h}$ is the combination of the central force, coriolis force, and gravity terms. On the right side of Eq. (1), $\boldsymbol{J}_c^{\mathrm{T}}\boldsymbol{\lambda}$ is the holonomic constraint. $\boldsymbol{J}_T^{\mathrm{T}}\boldsymbol{F}_T$ is the tension due to soft cable.

Additionally, as represented by Eq. (2), it is assumed that there is no friction on the ground, and both the front and the rear rimless wheel have a limb in contact with the ground. Therefore the velocity constraint equation is shown as follows:

$$\dot{x}_r = 0, \quad \dot{z}_r = 0, \quad \dot{x}_f = 0, \quad \dot{z}_f = 0. \tag{3}$$

By summarizing Eq. (3), we can obtain constraint Jacobian matrix $\boldsymbol{J}_c$ as:

$$\boldsymbol{J}_c = \begin{bmatrix} 1\,0\,0\,0\,0\,0\,0\,0 \\ 0\,1\,0\,0\,0\,0\,0\,0 \\ 0\,0\,0\,0\,1\,0\,0\,0 \\ 0\,0\,0\,0\,0\,1\,0\,0 \end{bmatrix}, \quad \dot{\boldsymbol{J}}_c = \boldsymbol{0}_{4\times 8}. \tag{4}$$

The time derivative of Eq. (2) becomes:

$$\boldsymbol{J}_c\ddot{\boldsymbol{q}} = \boldsymbol{0}_{4\times 1}, \tag{5}$$

and by solving Eq. (5) and Eq. (1), $\boldsymbol{\lambda}_c \in \mathbb{R}_{4\times 1}$ can be obtained as:

$$\boldsymbol{\lambda}_c = -\boldsymbol{X}_c^{-1}\boldsymbol{J}_c\boldsymbol{M}^{-1}(\boldsymbol{J}_T^{\mathrm{T}}\boldsymbol{F}_T - \boldsymbol{h}), \tag{6}$$

$$\boldsymbol{X}_c = \boldsymbol{J}_c\boldsymbol{M}^{-1}\boldsymbol{J}_c^{\mathrm{T}}. \tag{7}$$

C. Tension

Fig. 3 shows the details of the soft cable connection. Each connection point subjected tension from two different directions on upper body, the model has total four spring connections, the effect of the tension force vector on the robot can be defined as:

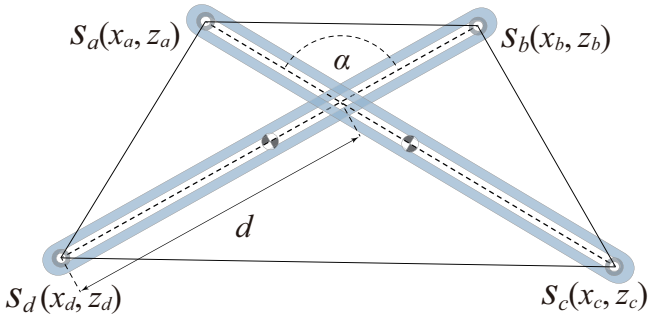

Fig. 3. The detail of spine. In this figure α is the angle between the upper body, d is the distance from the bottom of upper bodies to their point of intersection.

$$\boldsymbol{J}_T^{\mathrm{T}}\boldsymbol{F}_T = \begin{bmatrix}\boldsymbol{J}_1^{\mathrm{T}} & \boldsymbol{J}_2^{\mathrm{T}} & \dots & \dots & \boldsymbol{J}_7^{\mathrm{T}} & \boldsymbol{J}_8^{\mathrm{T}}\end{bmatrix} \begin{bmatrix} F_1 \\ F_2 \\ \cdots \\ \cdots \\ F_7 \\ F_8 \end{bmatrix}. \tag{8}$$

The tension of the whole system consisted of 4 soft cable, and the connection order is: $S_a \to S_b, S_b \to S_c, S_c \to S_d, S_d \to S_a$, where the letter S represents the soft cable. We take an element from matrix (8) as a example: $\boldsymbol{J}_1^{\mathrm{T}}\boldsymbol{F}_1$ represents the tension applied at point S_{bB} , and its tension can be described as:

$$\boldsymbol{J}_1^{\mathrm{T}}\boldsymbol{F}_1 = \boldsymbol{J}_a^{\mathrm{T}} F_{S_a \to S_b}, \tag{9}$$

where $\boldsymbol{J}_a$ is the Jacobain vector of connection point S_a on upper body of front rimless wheel. The $\boldsymbol{d}_{S_a \to S_b}$ represents the direction vector from connection point $S_a \to S_b$. The details are shown as follows:

$$\boldsymbol{J}_a = \begin{bmatrix} 0\,0\,0\,0\,1\,0 & R_f\cos\theta_f & L_f\cos\gamma_f \\ 0\,0\,0\,0\,0\,1 & -R_f\sin\theta_f & -L_f\sin\gamma_f \end{bmatrix} \tag{10}$$

$$\boldsymbol{d}_{S_a \to S_b} = \boldsymbol{P}_{S_a \to S_b} / D_{S_a \to S_b}. \tag{11}$$

The (x_a, z_a) and (x_b, z_b) in Fig. 3 represent the coordinate of connection point S_a and S_b respectively, so the displacement vector and distance can be obtained as:

$$\boldsymbol{P}_{S_a \to S_b} := \begin{bmatrix} x_b - x_a \\ z_b - z_a \end{bmatrix}, \tag{12}$$

$$D_{S_a \to S_b} := \sqrt{(x_b - x_a)^2 + (z_b - z_a)^2}, \tag{13}$$

$$F_{S_a \to S_b} = k(D_{S_a \to S_b} - l_n) + c\boldsymbol{V}_{S_a \to S_b}^{\mathrm{T}} \boldsymbol{d}_{S_a \to S_b}, \tag{14}$$

$$\boldsymbol{V}_{S_a \to S_b} := \begin{bmatrix} \dot{x}_b - \dot{x}_a \\ \dot{z}_b - \dot{z}_a \end{bmatrix}, \tag{15}$$

where k [N/m] and c [N·s/m] are stiffness and viscosity coefficient of soft cable, respectively. The l_n is nature length of the soft cable.

D. Collision Equation

It is assumed that when the fore limb of both rimless wheels impact to the ground, the rear limb will leave the ground immediately according to the inelastic collision model. The holonomic constraint equation after impact can be formulated as follows.

$$\boldsymbol{M}\dot{\boldsymbol{q}}^+ = \boldsymbol{M}\dot{\boldsymbol{q}}^- + \boldsymbol{J}_I^{\mathrm{T}}\boldsymbol{\lambda}_I, \tag{16}$$

$$\boldsymbol{J}_I\dot{\boldsymbol{q}}^+ = \boldsymbol{0}_{2\times 1}. \tag{17}$$

Here, the superscripts "−" and "+" denote immediately before and immediately after impact, respectively. The $\boldsymbol{J}_I$ is the Jacobian vector of constrain force at collision, then the constrained condition is

$$\dot{x}_I^+ = 0, \quad \dot{z}_I^+ = 0, \tag{18}$$

and can be further arranged as follows:

$$\boldsymbol{J}_I\dot{\boldsymbol{q}}^+ = \begin{bmatrix} 1\,0 & R_f(\cos\theta_f + \cos\theta_f) & 0\,0\,0\,0\,0 \\ 0\,1 & -R_f(\sin\theta_f + \sin\theta_f) & 0\,0\,0\,0\,0 \end{bmatrix} \dot{\boldsymbol{q}}^+ = 0. \tag{19}$$

By solving Eq. (16) and (17) , the $\boldsymbol{\lambda}_I$ can be derived as:

$$\boldsymbol{\lambda}_I = -\boldsymbol{X}_I^{-1}\boldsymbol{J}_I\dot{\boldsymbol{q}}^-, \boldsymbol{X}_I = \boldsymbol{J}_I\boldsymbol{M}^{-1}\boldsymbol{J}_I^{\mathrm{T}}. \tag{20}$$

The velocity vector immediately after impact can be obtained as:

$$\dot{\boldsymbol{q}}^+ = \left(\boldsymbol{I}_8 - \boldsymbol{M}^{-1}\boldsymbol{J}_I^{\mathrm{T}}\boldsymbol{X}_I^{-1}\boldsymbol{J}_I\right)\dot{\boldsymbol{q}}^-. \tag{21}$$

III. GAIT ANALYSIS

A. Design of the Spine Structure

Before initiating the analysis, the author would like to clarify the design approach for the shape of the spine, which is composed of soft cables and upper bodies.

First, we assume that the spine structure, as shown in the Fig. 3, is symmetrical. The upper body lengths of the two rimless wheel are identical and are considered constant are chosen as the same values as listed in Table I. By determining the angle α [deg] between the upper body and the distance d [m] from the bottom of upper bodies to their point of intersection, the side lengths of the isosceles trapezoid formed by the soft cables can be solved by geometric relations. This method streamlines the process of determining the shape of the spine structure. In other words, by simply determining the angle α and the d, the shape of the spine structure in its balance state can be defined.

To investigate the influence of the spine on walking performance, we developed a simulator and chose walking speed as the metric for evaluating performance. It is set up the simulation time for 40 seconds and only take the simulation result of last 10 steps, because we want to ensure the data obtained is reaching the stable walking cycle. The initial state of robot started passive dynamic walking as shown in matrix (22):

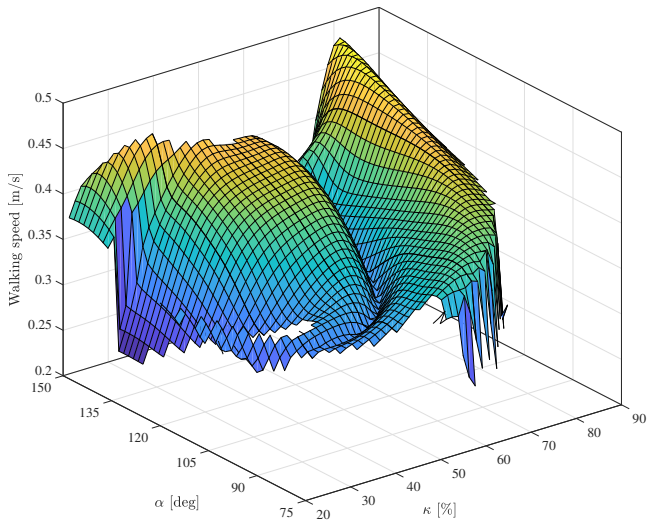

(a) 3D-surface of walking speed with respect to α and κ

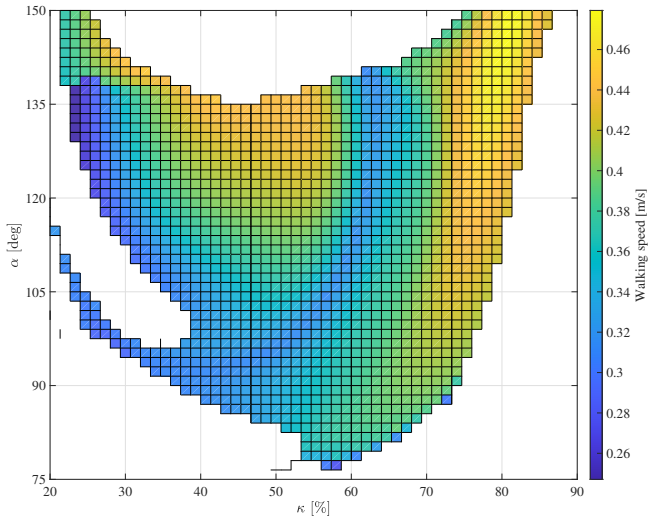

(b) Top-down view of walking speed with respect to α and κ

Fig. 4. Simulation results of walking speed under various values α and κ

$$\boldsymbol{q}(0) = \begin{bmatrix} 0 \\ 0 \\ 0 \\ \phi + \frac{\alpha}{2} \\ 2d\cos\phi\sin\frac{\alpha}{2} \\ -2d\sin\phi\sin\frac{\alpha}{2} \\ 0 \\ \phi - \frac{\alpha}{2} \end{bmatrix}, \quad \dot{\boldsymbol{q}}(0) = \begin{bmatrix} 0 \\ 0 \\ 2 \\ 0 \\ 0 \\ 0 \\ 2 \\ 0 \end{bmatrix}. \tag{22}$$

B. Motion analysis

Fig. 4 shows the simulation results of the walking speed descriptors in passive-dynamic walking with variable α and κ. To generalize the model, here, κ is used to represent the ratio between d [m] and the length of upper body L_i [m], so the ratio of κ can be obtained as:

$$\kappa = d/L_i. \tag{23}$$

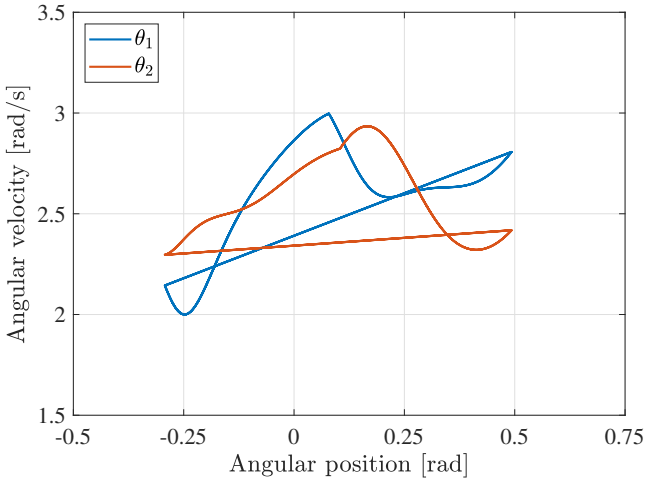

Fig. 5. Steady-state phase-plane plot

The physical parameters are chosen as the same values as listed in Table I. Fig. 4(a) shows the three-dimensional surface plot, which shows most of the surface appears relatively smooth. However, there is a pronounced valley around α=120 [deg] and κ=60% is found, whose data in the valley region represents a collection of spine structures that resulted in weak walking speeds. Conversely, the graph also showcases two peaks near α=135 [deg], κ=46.7% and α=150 [deg], κ=80%. These peaks represent configurations where the better walking performance under same specific physical parameters.

Fig. 4(b) is the plan view of the three-dimensional graph. The horizontal axis represents the ratio κ between d [m] and L_i [m], while the vertical axis denotes the angle α [deg] between the upper body. The color intensity at each point signifies the magnitude of the value, with the variations in magnitude being illustrated through the color bar on the right side. The blank areas in the figure indicate situation where walking failed under those parameter combinations. The failures in the upper-middle part are due to the insufficient tension produced by the soft cables, leading to the collapse of the entire spine structure. The failures located in the bottom-right section of the figure are due to excessive energy consumption within the spine in these particular configurations. The remaining energy was insufficient to support the energy requirements for passive walking, ultimately leading to the cessation of locomotion. The failures in the bottom-left section of the figure are due to the excessively high center

TABLE I
PHYSICAL PARAMETERS OF SYSTEM

Symbol	Value	Unit	Symbol	Value	Unit
$m_r = m_f$	0.5	kg	g	9.81	m/s^2
$I_r = I_f$	0.0625	kg·m^2	ϕ	0.1	rad
$R_r = R_f$	0.5	m	k	500	N·m
$L_r = L_f$	1.5	m	c	5	N·s/m

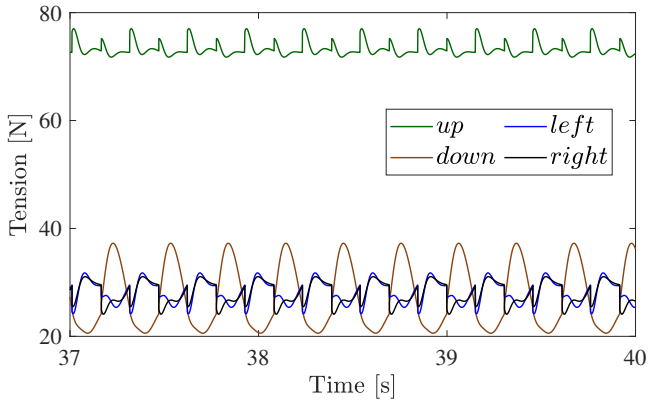

(a) Tensions on the 4 edges of the spine

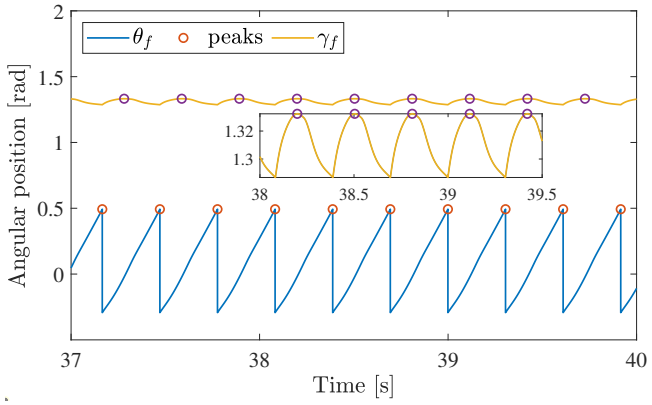

(b) Angular position of θ_f and γ_f

Fig. 6. Simulation results during last 3 seconds on the peak of Fig. 4(a)

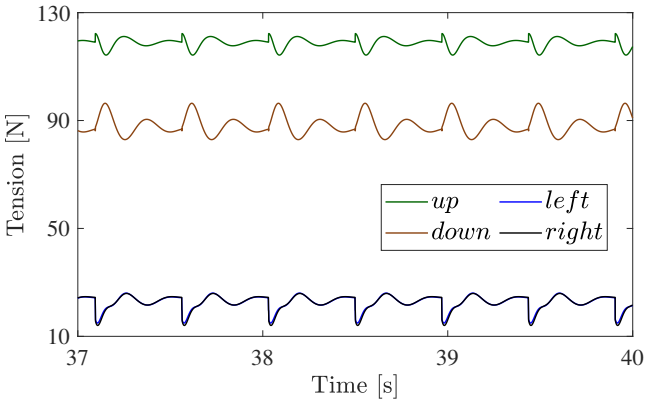

(a) Tensions on the 4 edges of the spine

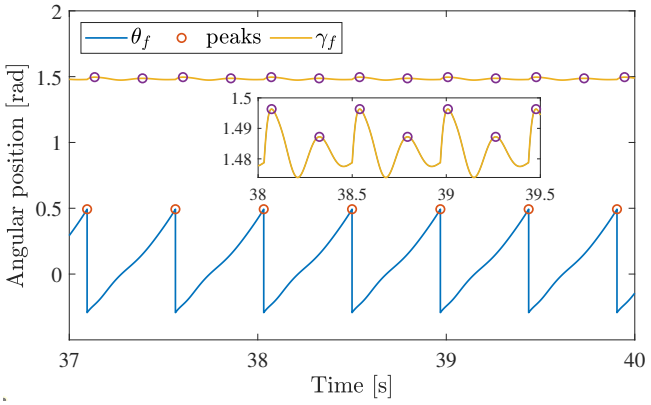

(b) Angular position of θ_f and γ_f

Fig. 7. Simulation results during last 3 seconds on the valley of Fig. 4(a)

of gravity of the spine in that specific configuration, causing it to tip forward or backward during walking.

Fig. 6 shows the tension on the four edges of the spine during the last 3 seconds of a 40-second simulation (a), as well as the time evaluation angle position for both the fore rimless wheel and its upper body (b) at the best performance point in Fig. 4, where α=150 [deg] and κ=80%. In Fig. 6(a), it is illustrated that the tension acting on the upper body shows periodic fluctuations. Under the influence of this force, the upper body also undergoes periodic changes. Fig. 6(b) shows the detailed of upper body's angle changes from 38 seconds to 39.5 seconds. Furthermore, the observation shows that when the γ_f curve reaches a trough, the θ_f is precisely at peak.

Fig. 7 shows the simulation results of the last 3 seconds for the point in Fig. 4 from valley, that exhibited the weak walking performance. Comparing to Fig. 6, it can be observed that in this case, the internal tension acting on the spine have significantly increased. Additionally, the waveform of the angle γ_f of upper body exhibits a double periodicity, whereas Fig. 6 (b) showed a single periodicity. The authors speculate that such variations in the spine's frequency might influence walking performance.

On the other hand, to investigate the impact of the spine's weight on locomotion, the walking speed is used as an evaluation criterion and the proportion of leg weight to spine weight as the horizontal axis, conducted simulations under different stiffness k [N/m] of soft cable. The simulation results as shown at Fig. 8. The figure demonstrates that in most cases, the combined rimless wheel with a spine structure can achieve stable single-period walking. Only when k=200 [N/m], as the proportion of leg weight to spine weight gradually increases, the walking gaits start to occur double-period and multi-period walking, indicating that decreasing gait stability. Furthermore, the simulation results suggest that the walking performance is better when the proportion of leg weight to spine weight is lower.

IV. DISCUSSION

The combined rimless wheel with a spine structure composed of soft cables and a rigid upper body can achieve stable dynamic walking on a gentle slope. Moreover, the walking performance can be adjusted based on the shape of the spine. In this study, we observed periodic vibrations occurring in the upper body as a part of the spine, and there seems to be a potential relationship between the vibration frequency and the walking performance. Such observations can provide insights into the biomechanics of the structure and further aid in optimizing the design for better functionality and efficiency. The author speculates that leveraging the spinal structure to achieve resonance between the upper body and the rimless wheel could effectively enhance walking performance, but

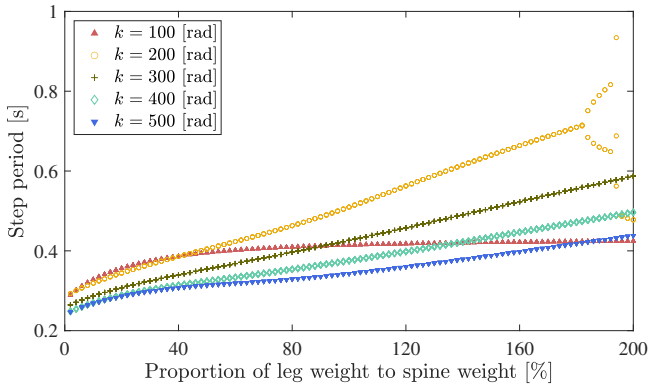

(a) Step period

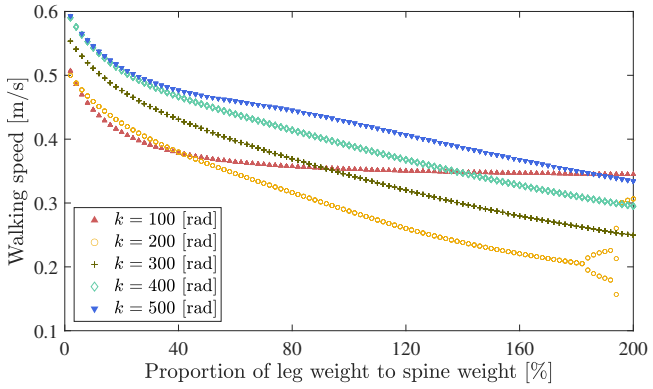

(b) Walking speed

Fig. 8. Simulation results with respect to proportion of leg weight to spine weight

further validation is needed.

V. CONCLUSION AND FUTURE WORK

This study designed a linked wheel model with a spine. Through observing the passive walking of the proposed model, we discovered that it can achieve stable passive walking. We also observed the trend of walking performance under the influence of the spine. This has made a contribution to the design of mobile robot structures. The authors hope to use this model to study the locomotion mechanism of quadruped robots and enhance their mobility performance, and also like to provide insights into the biomechanics of the structure and further aid in optimizing the design for better functionality and efficiency.

In the future, from the mechanistic perspective, the relationship between the vibration frequency of the spine and walking performance will be discussed in-depth. From the application standpoint, we aim to achieve walking on flat ground by controlling the spine, and to develope highly efficient mobile robots that able to use the advantages on spine. By utilizing the locomotion characteristics of the spine we found, we hope to enhance its mobility and increase its practicality for tasks like reconnaissance and exploration in special scenarios. Ultimately, we will conduct experiments to verify the feasibility, practicality, and effectiveness of this model.

REFERENCES

[1] R. M. Alexander, N. J. Dimery, and R. F. Ker, "Elastic structures in the back and their rôle in galloping in some mammals," *Journal of Zoology*, vol. 207, no. 4, pp. 467–482, 1985.

[2] M. Hildebrand, "Motions of the Running Cheetah and Horse," *Journal of Mammalogy*, vol. 40, no. 4, pp. 481–495, 1959.

[3] P. Eckert, A. Spröwitz, H. Witte, and A. J. Ijspeert, "Comparing the effect of different spine and leg designs for a small bounding quadruped robot," in *2015 IEEE International Conference on Robotics and Automation (ICRA)*, 2015, pp. 3128–3133.

[4] Y. Tang, Y. Chi, J. Sun, T.-H. Huang, O. H. Maghsoudi, A. Spence, J. Zhao, H. Su, and J. Yin, "Leveraging elastic instabilities for amplified performance: Spine-inspired high-speed and high-force soft robots," *Science Advances*, vol. 6, no. 19, 2020.

[5] Q. Zhao, B. Ellenberger, H. Sumioka, T. Sandy, and R. Pfeifer, "The effect of spine actuation and stiffness on a pneumatically-driven quadruped robot for cheetah-like locomotion," in *2013 IEEE International Conference on Robotics and Biomimetics (ROBIO)*, 2013, pp. 1807–1812.

[6] J. Duperret and D. E. Koditschek, "Empirical validation of a spined sagittal-plane quadrupedal model," in *2017 IEEE International Conference on Robotics and Automation (ICRA)*, 2017, pp. 1058–1064.

[7] R. J. Kowalski, L. A. Ferrara, and E. C. Benzel, "Biomechanics of the spine," *Neurosurgery Quarterly*, vol. 15, pp. 42–59, 2005.

[8] R. Izzo, G. Guarnieri, G. Guglielmi, and M. Muto, "Biomechanics of the spine. part i: spinal stability." *European journal of radiology*, vol. 82 1, pp. 118–26, 2013.

[9] C. Paul, F. Valero-Cuevas, and H. Lipson, "Design and control of tensegrity robots for locomotion," *IEEE Transactions on Robotics*, vol. 22, no. 5, pp. 944–957, 2006.

[10] A. P. Sabelhaus, J. Bruce, K. Caluwaerts, P. Manovi, R. F. Firoozi, S. Dobi, A. M. Agogino, and V. SunSpiral, "System design and locomotion of superball, an untethered tensegrity robot," *2015 IEEE International Conference on Robotics and Automation (ICRA)*, pp. 2867–2873, 2015.

[11] D. Zappetti, R. Arandes, E. Ajanic, and D. Floreano, "Variable-stiffness tensegrity spine," *Smart Materials and Structures*, vol. 29, no. 7, p. 075013, 2020.

[12] S. Levin, "The tensegrity-truss as a model for spine mechanics: Biotenseglrity," *Journal of Mechanics in Medicine and Biology*, vol. 02, 2011.

[13] R. M. Alexander and A. Jayes, "Optimum walking techniques for idealized animals," *Journal of Zoology*, vol. 186, no. 1, pp. 61–81, 1978.

[14] R. M. Alexander, "Optimum walking techniques for quadrupeds and bipeds," *Journal of Zoology*, vol. 192, no. 1, pp. 97–117, 1980.

[15] T. M. Griffin, R. P. Main, and C. T. Farley, "Biomechanics of quadrupedal walking: how do four-legged animals achieve inverted pendulum-like movements?" *Journal of Experimental Biology*, vol. 207, no. 20, pp. 3545–3558, 2004.

[16] T. McGeer, "Passive dynamic walking," *The International Journal of Robotics Research*, vol. 9, no. 2, pp. 62–82, 1990.

[17] F. Asano, M. Yamakita, and K. Furuta, "Virtual passive dynamic walking and energy-based control laws," in *2000 IEEE/RSJ International Conference on Intelligent Robots and Systems (IROS)*, vol. 2, 2000, pp. 1149–1154.